Converted-wave (*P-SV*) data processing and interpretation for 3-D surveys: a physical modeling example

Don C. Lawton and Shaowu Wang

ABSTRACT

Including converted-wave (*P-SV*) data in seismic programs can provide for a more fully integrated interpretation than that obtainable from *P-P* data alone. Physical modeling has proved to be a very useful way to evaluate experimental design, data processing algorithms and interpretation methods for 3-D converted-wave survey. With the aid of a 3-D converted-wave data set over a 3-D physical model, an isotropic 3-D processing flow for converted-waves was developed. Due to the asymmetry of the *P-SV* raypath, data processing differs from that for *P-P* waves and involves special processes, such as component rotation, *P-SV* NMO correction and common conversion point (CCP) binning.

Comparison of *P-P* and *P-SV* migrated sections from a sample physical model showed very good correspondence. However, although the model is symmetric in the receiver-line direction, *P-SV* events were found to be asymmetric over the flanks of the model, probably because of the asymmetry of *P-SV* raypaths and the particular design of the survey. The application of single-pass phase-shift migration proved to be successful for migrating the converted-wave data, given a good stacked section and an accurate velocity estimation.

INTRODUCTION

The acquisition, processing and interpretation of *P*-wave 3-D seismic data has been fully developed in recent years. However, for converted-waves (*P-SV*), the 3-D processing flow is in early development. The interpretation of *P-SV* data can not only enhance the interpretation results of *P*-wave data, but can also provide independent information, such as another image of the subsurface, and illuminate an interface, which may not have a *P*-wave velocity contrast, but which may have an *S*-wave velocity contrast. Including *P-SV* data into our interpretation may lead to a fully integrated interpretation of structure, lithology, porosity and reduction in the risk of finding hydrocarbons (Tatham et al., 1976; Tatham, 1982; Tatham et al., 1983; Tatham et al., 1984; Tatham et al., 1994).

As shown in Figure 1, for an isotropic medium with a flat reflector, the *P-P* raypath is symmetric, whereas the *P-SV* raypath is asymmetric due to the fact that the *S*-wave velocity is lower than the *P*-wave velocity. Moreover, their polarization directions are also different; for *P*-waves it is in the direction of the raypath, whereas for *S*-waves it is perpendicular to its raypath. Hence, for three-dimensional (3-D) and three-component (3-C) data acquisition, not only the vertical component, but also the in-line (receiver-line) and cross-line (shot-line) horizontal components are recorded, in order to obtain radial and transverse components with respect to the source-receiver azimuth. For conventional *P-P* recording, source-receiver offsets can be from zero-
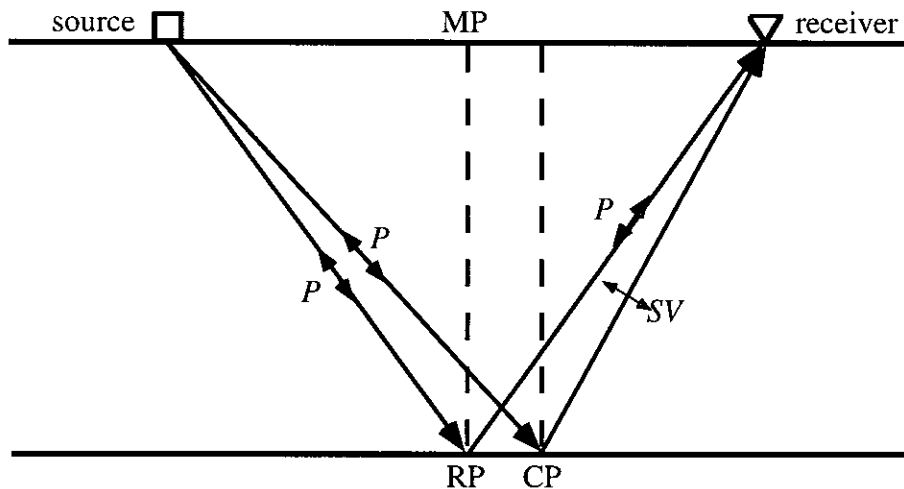
FIG. 1. Diagram of *P-P* wave and *P-SV* wave ray paths. RP: *P-P* reflection point. CP: *P-SV* conversion point.

offset to reasonably large offsets, but for mode-converted (*P-SV*) waves, data with moderate offsets are most useful (Lawton, 1992), according to the principle of partitioning of wave energy on a reflector.

After data have been collected from a field survey or from a physical modeling experiment, correct processing procedures are important to obtain the optimum image of the subsurface. Due to the asymmetry of *P-SV* raypaths, data acquisition and processing for *P-SV* data differ from that for pure *P*-wave data. The key step in 3-D *P-SV* data processing is the concept of common conversion point (CCP) binning. Asymptotic CCP stacking and depth-variant CCP stacking for 2-D converted-wave surveys have been developed by the CREWES Project in recent years (Eaton et al., 1989). For 3-D converted-wave surveys, azimuth has to be taken into account in CCP binning. In order to enhance *P-SV* wave energy and improve signal-to-noise ratio to obtain good stacked data, component rotation (Lane et al., 1993), converted-wave NMO (Slotboom et al, 1990) and modal separation of *P-P* wave energy and *P-SV* wave energy (Dankbaar, 1985; Lane et al., 1993) are applied.

Numerical simulation and/or physical modeling are often used to evaluate the feasibility of experimental design and data processing without the cost of field acquisition (Chen et al., 1993; Ebrom et al., 1990; Chon et al., 1990). Physical modeling is a very useful way to evaluate experimental design, data processing algorithms and interpretation methods in that the model and acquisition geometry are controlled, yet the data have many of the characteristics of field data (Chen et al., 1993). In physical modeling, discretization in numerical modeling is not needed, approximations and assumptions may be avoided, and roundoff errors need not accumulate. Furthermore, compared to numerical modelling methods, physical models suffer from all of the experimental errors that plague actual field work, such as positioning uncertainties, dynamic-range limitations and undesired (but real) interfering events (Ebrom et al., 1990).

In this work, with the aid of a 3-D *P-SV* physical modeling dataset over a three-dimensional model, we develop a 3-D data processing flow for converted-waves and compare the interpretation of the *P-P* and *P-SV* processed data volumes.

MODEL DESCRIPTION

The 3-D physical model consists of a rectangular-shaped cavity milled into the base of a layer of plexiglas 9.8 cm thick; Plexglas has a P-wave velocity of 2750 m/s and an S-wave velocity of 1375 m/s. Cross-sections showing the geometry of the model are shown in Figure 2. The cavity is about 1.4 cm deep, 8.0 cm long, 5.0 cm wide and is air-filled. As seen in Figure 2, the model is symmetric in the in-line (receiver-line) direction and asymmetric in the cross-line (shot-line) direction. Other parameters about the model are shown in Figure 2. World units are shown using a distance scaling factor of 10,000:1. A time scaling factor of 10,000:1 and a velocity scaling factor of 1:1 were used to convert from experimental to world units.
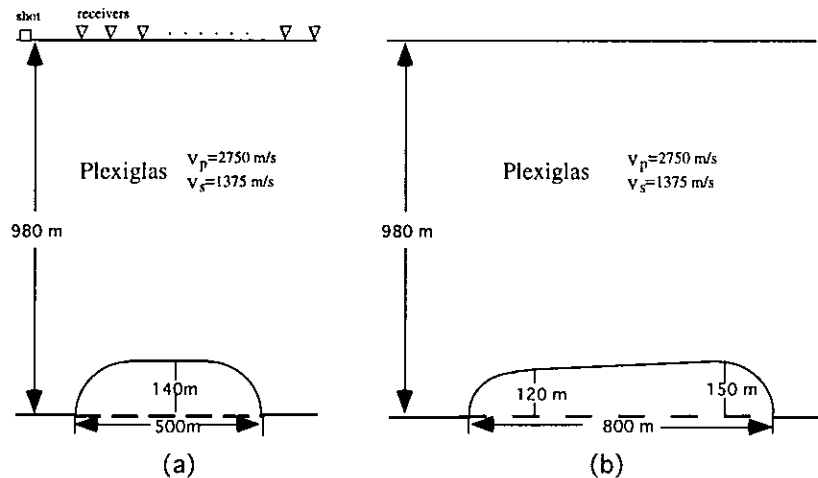
FIG. 2. Cross-sections of the model in receiver-line (a) and shot-line (b) directions across the center of the model.
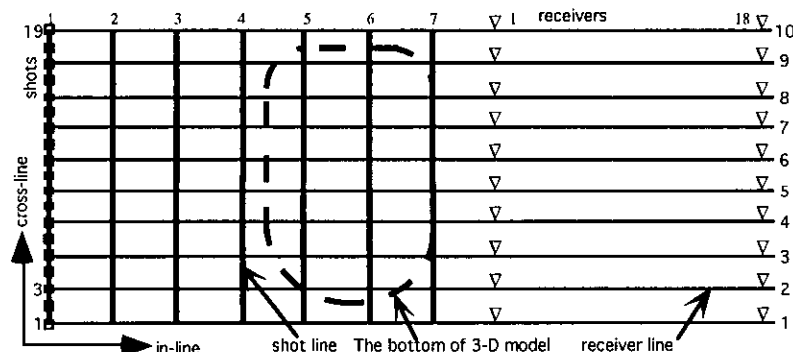
FIG. 3. Plan view of model showing acquisition geometry. Receiver locations are indicated for shot line 7.

DATA ACQUISITION

A three-dimensional, three-component dataset was acquired over the model using a P-wave transducer as the source. A plan view of the survey is shown in Figure 3. All dimensions and parameters are referred to in world units. There were 7 shot lines recorded with line spacing of 200 m, 19 shots per shot-line and shot spacing of 50 m. For each shot, data were acquired along 10 receiver lines with a spacing of 100 m,

a near offset of 200 m, 18 receiver stations per receiver line and a receiver spacing of 50 m. Each shot line lay 200 m from the active receiver patch. The sample interval was 1 ms and the record length was 1.5 s. The survey was repeated three times to enable vertical, in-line and cross-line receiver components to be collected. Here, in-line refers to receiver line direction and cross-line refers to shot-line direction.

Figure 4a is an example of the collected data, showing a shot gather for the in-line receiver component with a *P*-wave source located at station 9 of shot line 1. The receivers for this gather were along receiver line 5; i.e. the shot and receivers lie in the same plane. For this shot gather, which is located over the flat part of the model, the main reflection events are the *P-SV* (event 2) and *P*-wave leakage (event 1) from the flat interface at the bottom of the model. By carefully examining event 2, it is clear that for near-offset traces, *P-SV* amplitudes are smaller than traces with medium offsets. This is because at small offsets, the *P*-wave incident angle is small, and mode-converted energy is weak according to the principle of partitioning of energy at an interface.
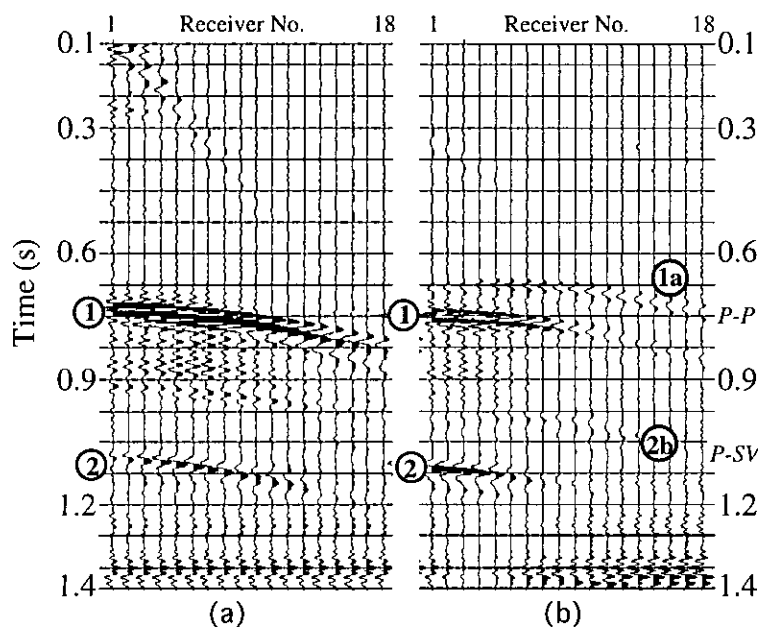

FIG. 4. Example of data collected for in-line receivers.
(a) Shot station 9, shot-line 1 and receiver-line 5
(b) Shot station 9, shot-line 3 and receiver-line 5

Figure 4b shows another in-line component shot gather with a *P*-wave source at station 9 of shot line 3. The receivers are still along receiver line 5, but now cover the structured part of the model. In this figure, events 1 and 1a are the *P*-wave leakage from the flat interface and the top of the 3-D model respectively, whereas events 2 and 2a are *P-SV* reflections from the flat basal interface and the top of the cavity respectively.

DATA PROCESSING

Although 3C-3D data were collected, the primary interest in this experiment is the 3-D *P-SV* data processing and interpretation. However, for the purpose of comparison, the *P-P* wave dataset was also processed using a conventional 3-D
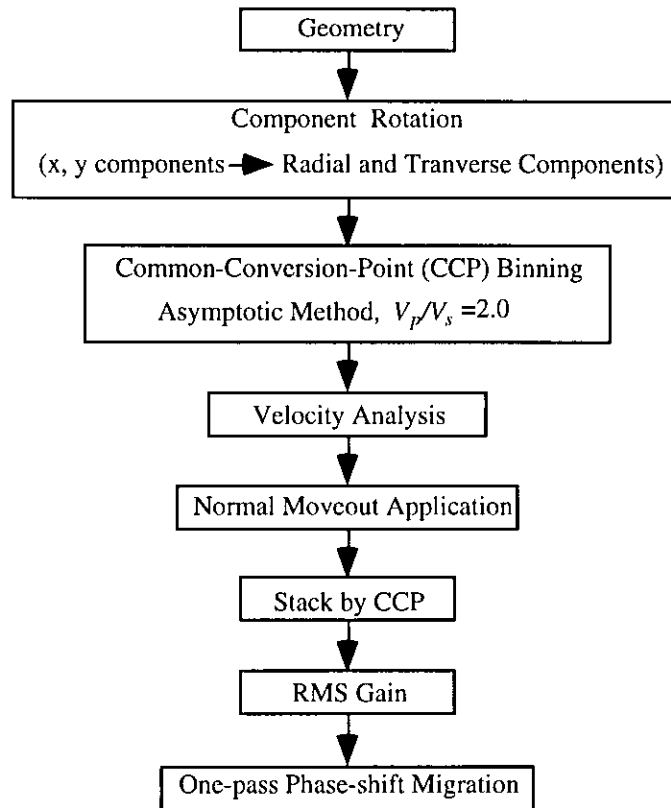
FIG. 5. Flow chat for 3-D isotropic *P-SV* processing.

processing flow. The processing flow chart developed for isotropic 3-D *P-SV* data is shown in Figure 5. Some special processes, such as component rotation, *P-SV* NMO correction and common conversion point (CCP) binning were applied. Component rotation (Lane et al., 1993) was applied to transfer the in-line and cross-line components into radial and transverse components for each source-receiver azimuth. Asymptotic common conversion point (CCP) binning proved to be an adequate binning method for this dataset since the depth of interest is quite large compared to the offset range. A *P-SV* NMO correction (Slotboom et al, 1990) was also implemented.
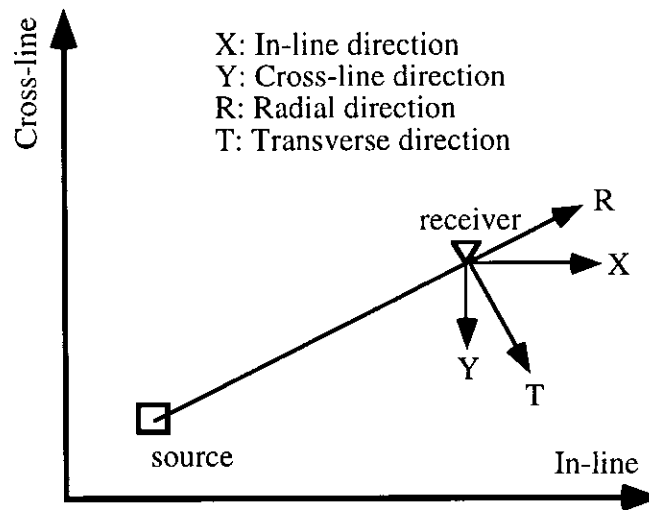
FIG. 6. Plan view of component rotation.

As shown in Figure 6, after recording two horizontal components for each source-receiver azimuth (in-line (X) and cross-line (Y) components), the data were rotated into radial and transverse components with respect to the source-receiver azimuth. The rotation was undertaken so that *P-P* events on the processed vertical component were of the same polarity as the *P-SV* events on the processed radial component. In the isotropic case, the radial component will contain only *P-SV* data while the transverse component should be nulled. Figures 7a and 7b are examples of data from in-line and cross-line component respectively for shot station 1 on shot line 1. In this example, only the data on the first 5 receiver lines are displayed. The *P-SV* event is between times 1.05 s and 1.25 s and this event can be seen not only on the in-line component but also on the cross-line component. With different source-receiver azimuths, the amplitudes of the *P-SV* event on different lines vary. With the receiver line number increasing, i.e. the receiver lines are away from the shot position and the source-receiver azimuths are increased, the *P-SV* energy in in-line component is weaker, whereas on cross-line component this event becomes stronger. After component rotation, it is clear that the *P-SV* energy is almost all on the radial component (Figure 8a), whereas that on the transverse component is very weak (Figure 8b). Ideally, the *P-SV* energy on the transverse component should be zero, but because of the large size of the transducer and minor positioning errors, some *P-SV* energy leaked onto the transverse component.

A key step in *P-SV* data processing is the common conversion point (CCP) binning. As shown in Figure 9, the conversion point lies between the source and receiver, but is displaced toward the receiver position from the midpoint. The exact location depends on V_p/V_s and on the depth of the conversion point (Eaton et al.,
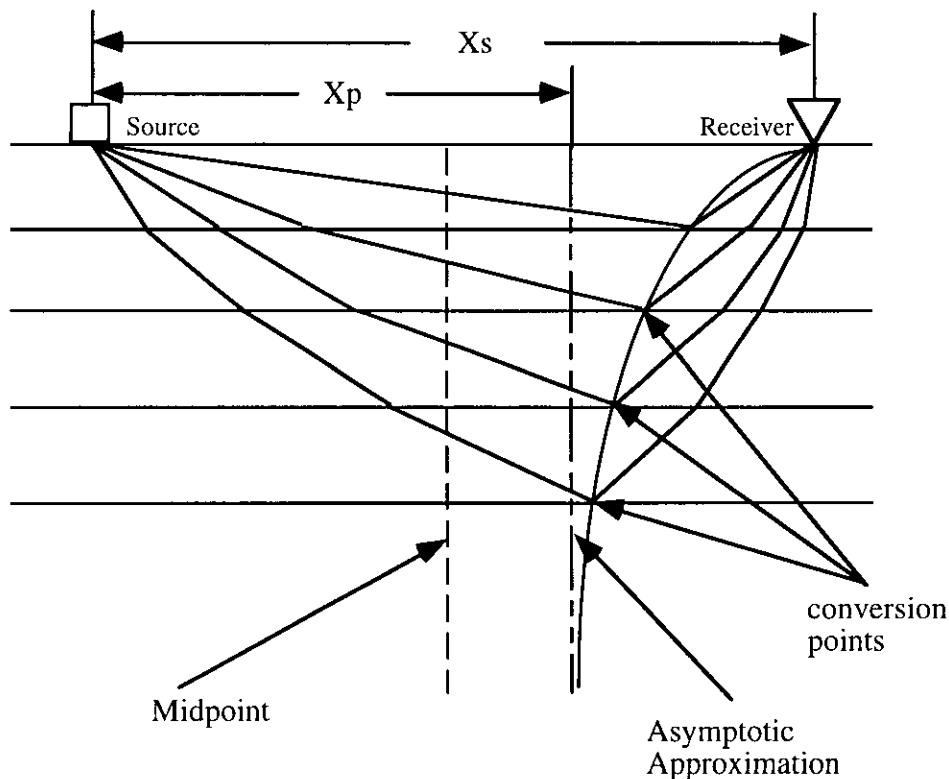

FIG. 9. Schematic diagram of asymptotic common conversion point (CCP) binning.

1990). However, if the ratio of offset to depth of interest is not very large, we may consider the asymptotic location as a first approximation for binning and stacking purposes. As denoted in Figure 9, the horizontal distance (Xp) of the asymptotic location away from the source is given by

$$X_p = \frac{X_s}{1 + V_s/V_p},$$

where X_s is the source-receiver offset and V_p and V_s are the P- and S-wave velocities respectively. For this experiment, the maximum horizontal position error between asymptotic common point and the true common point at the depth of interest is only 7 m, which is far smaller than the bin size (25 m).

The fold map for asymptotic CCP binning is shown in Figure 10. In this figure, the bin dimensions in in-line and cross-line directions are half of the receiver interval, and half of the shot interval, respectively (25 m). From this fold map, it is seen that every fourth row in the receiver-line direction is empty. This is because when a conventional common midpoint bin size of half the receiver interval $(\Delta r/2)$ is used, the fold distribution is highly variable and empty rows of bins parallel to the shot lines may result for the case when $V_p/V_s=2$ and the shot line spacing is an even integer multiple of Δr (Lawton, 1993). To overcome this problem, the optimum bin size in asymptotic CCP binning is proposed by Lawton (1993). In this method, the optimum bin size ΔX_c was given by:

$$\Delta X_c = \frac{\Delta r}{1 + V_s/V_p}.$$

So, for this physical modeling dataset, $\Delta r=50m$, $V_s/V_p=0.5$, and here the optimum bin size ΔX_c is 33.3 m. The fold map using asymptotic CCP binning with the optimum bin size is shown in Figure 11, in which the fold distribution is much more even than that with a bin size of 25 m and the empty bins have disappeared.

Before stacking, correction for normal moveout (NMO) was applied to the dataset. The P-SV NMO curve differs from P-P NMO curve. The standard hyperbolic NMO formula has limited application to converted-wave NMO, particularly when data with high offset-to-depth ratio are used. Therefore, a time-shifted hyperbolic NMO formula (Slotboom, et al., 1990) was applied,

$$t = \frac{t_0}{2} + \sqrt{\frac{t_0^2}{4} + \frac{X_s^2}{2V_{ps}^2}},$$

where V_{ps} is the effective P-SV stacking velocity. For a constant velocity model, it has the form of $V_{ps}=\sqrt{V_p V_s}$. Figures 12 and 13 show examples of NMO-corrected data using teh standard hyperbolic equation and time-shifted hyperbolic equation. Carefully examining the P-SV event, we can see that the result of using time-shifted hyperbolic equation with effective P-SV stacking velocity is only slightly better than that when the standard hyperbolic equation is used. This is because the offset-to-depth ratio in this case is not very large, so both of these methods will provde good results.

Figure 14 shows an example section of *P-SV* stacked data in the receiver-line direction, gathered with a bin size of 25 m. For every four traces, there is an empty trace. After linear interpolation of these empty traces, the results are shown in Figure 15. When the optimum bin size of 33.3 m is used in the asymptotic CCP binning, an example section of *P-SV* stacked data is shown in Figure 16, in which there are no empty traces, but the trace interval is greater than half of the receiver interval. After resampling the *P-SV* stacked data with optimum bin size of 33.3 m (Figure 16) into that with bin size of 25 m, the resulting section is shown in Figure 17. In order to quantitatively compare the difference between these two methods, the data in Figure 15 were subtracted by that in Figure 17. The result is shown in Figure 18, in which it is seen that the differences are very small. Hence in data with high S/N and events with small dip, the interpolation of empty bins using a conventional CMP bin size is also the equivalent of using an optimum bin size and resampling after stack.

The migrated section for *P-SV* stacked data shown in Figure 15 is shown in Figure 19. A single-pass phase-shift migration was applied to the *P-SV* stacked data using a migration velocity of $(v_p v_s)^{1/2}$. Figure 20 is a migrated section of the stacked data shown in Figure 17, in which the *P-SV* data were stacked with optimum bin size of 33.3 m, and then resampled into a bin size of 25 m. Later, the data in Figure 19 are subtracted by that in Figure 20, the difference is shown in Figure 21, in which it is seen that the difference between the migrated results of these two different processing flows is small. For comparison, the *P-P* data were also processed, using a conventional processing flow. The same receiver-line stacked section as in Figure 15 is shown in Figure 22 and the migrated section for Figure 22 is shown in Figure 23.

Based on above results, it is clear that single-pass phase-shift migration indeed collapsed the diffractions on the stacked section, and migration algorithm for *P-P* processing is suitable for *P-SV* processing given a good stacked section and an accurate velocity estimation.

INTERPRETATION

From the *P-SV* stacked section shown in Figure 15, it is clear that processed 3-D *P-SV* data did successfully yield good reflections corresponding to the 3-D model and the base of the plexiglas layer. Comparison of the *P-SV* (Figure 15) and *P-P*(Figure 22) stacked sections showed a very good correspondence between *P-SV* and *P-P* events. However, for both *P-P* and *P-SV* sections, the processed sections did not yield good events corresponding to the flanks of the cavity. This is mainly because of spatial aliasing, especially at the lower parts of the flanks where the dip angles reach 90 degrees. 3-D dip moveout (DMO) may assistant this imaging problem, especially at the positions where the dip angles are not very large.

From the sections in Figures 22 and 23, it is seen that the *P-P* events are almost symmetrical in the receiver-line direction. This is expected since the model is symmetrical in this direction (Figure 2). However, the events in the *P-SV* stacked and migrated sections (Figure 15 and Figure 19) are asymmetric. This is probably because of the asymmetry of downgoing *P*-wave and upgoing *S*-wave raypaths and the asymmetric geometry in the data acquisition.

Examples of time slices of stacked and migrated data are shown in Figures 24 and 25 for *P-P* data, and in Figures 26 and 27 for *P-SV* data respectively. The time

slices were chosen at times which conrrespond to the reflection from the top of the cavity in both *P-P* and *P-SV* data volumes. These times are 630 ms and 940 ms espectively. The time slice of *P-P* stacked data shows a very good symmetric image of the top of the cavity in the receiver-line direction. The exact position of the top of the model was obtained after migration. In Figure 26, the time slice of *P-SV* stacked data is asymmetric in the receiver-line direction. The migration in Figure 27 indeed collapsed the diffraction at the upper part of the left flank and gave a good image for the left edge of the top of the cavity, but the right edge of the model is poorly resolved, due to the reasons discussed above.

To compare the interpretation of the *P-P* and *P-SV* migrated data, horizon maps of the cavity were created (Figures 28 and 29) for *P-P* and *P-SV* data respectively. The mapped time intervals were chosen from 600 ms to 735 ms for *P-P* data, and from 900 ms to 1100 ms for *P-SV* data so that all of the reflection events of interest are in these time intervals. Because the velocity ratio of *P*-wave and *S*-wave is 2, for *P-SV* data, the time of an event corresponding to that in *P-P* section is 1.5 times larger than that for *P-P* data. The horizon map obtained from *P-P* migrated data is symmetrical in the receiver-line direction, because of the symmetry of the cavity in this direction and the symmetrical raypath of the *P-P* wave, whereas that from the *P-SV* migrated data is asymmetrical, due to the reasons disscussed above. The right flank of the cavity is poorly mapped, but the image of the left flank of the cavity from *P-SV* data is almost as good as that from *P-P* data. This means that *P-SV* data may have almost the same ability in imaging the substructures as *P-P* data have, provided the correct survey design and data processing.

CONCLUSIONS

(1) This study has shown that physical seismic modeling is a very useful way to evaluate experimental design and data processing algorithms for 3-D *P-SV* data.

(2) A 3C-3D dataset over a 3-D model was collected, which can not only be helpful for the development of processing flow and the design of the survey, but also be used to test other processing algorithms.

(3) Converted-wave data processing proved to be more complicated than that for either pure *P*-wave or pure *S*-wave data, and some special processes, such as component rotation, *P-SV* NMO correction, *P-SV* DMO and CCP binning must be applied.

(4) Component rotation successfully transferred the *P-SV* wave energy distributed in both in-line and cross-line components into radial component in the case of isotropic medium. Time-shifted hyperbolic equation with effective *P-SV* stacking velocity for *P-SV* NMO correction can improve the result of *P-SV* NMO application, even when the offset-to-depth ratio is large.

(5) Asymptotic common conversion point (CCP) binning proved to be a fast binning method and the horizontal position difference from the true conversion point can be small, when the depth of interest is large compared to the offset range. Compared with the CCP binning with conventional bin dimensions, the CCP binning method using optimum bin size can make the fold distribution more even and remove the empty bins. The interpolation of empty bins using a conventional CMP bin size is the equivalent of using an optimum bin size and resampling after stack.

(6) Because of the asymmetry of the *P-SV* raypaths and the particular design of this survey, converted-wave events in the receiver-line direction in both stacked and migrated sections were found to be asymmetrical over the flanks of the cavity, although the model in this direction is symmetrical.

(7) The application of 3-D migration made a significant improvement to the image of the cavity, and migration algorithm for *P-P* processing is suitable for *P-SV* processing given a good stacked section and an accurate velocity estimation. Further improvement in timaging of the flank of the cavity using *P-SV* data requires 3-D *P-SV* DMO or full prestack migration.

ACKNOWLEDGMENTS

REFERENCES

Chen, How-Wei, and McMechan, G.A., 1993, 3-D physical modeling of seismic common-source data volumes: Geophysics, 58, 121-133

Chon, Y.T., and Turpening, W.R., 1990, Complex salt and subsalt imaging: A seismic physical model study in 2-D and 3-D: 60th SEG, Expanded Abstracts, 1569-1571

Dankbaar, J.W.M., 1985, Separation of P and S waves: Geophys. Prosp., 33, 970-986

Eaton, D.W.S., and Stewart, R.R., 1989, Aspects of seismic imaging *P-SV* converted waves: CREWES project research report, v.1, 68-92

Eaton, D.W.S., Slotboom, R.T., Stewart, R.R., and Lawton, D.C., 1990, Depth variant converted wave stacking: 60th SEG, Expanded Abstract, 1107-1110

Ebrom, D.A., Tatham, R.H., Sekharan, K.K., McDonald, J.A., and Gardner G.H.F., 1990, Hyperbolic travel time analysis of first arrivals in an azimuthally anisotropic medium: A physical modeling study: Geophysics, 55, 185-191

Lane, M.C., and Lawton, D.C., 1993, 3-D converted wave asymptotic binning: CREWES project research report, v.5, 29-1-29-5

Lawton, D.C., Cheadle, S.P., Gallant, E.V., and Bertram, M.B., 1989, Elastic physical seismic modeling: CREWES project research report, v.1, 273-276

Lawton, D.C., 1993, Optimum bin size for converted-wave 3-D asymptotic mapping: CREWES project research report, v.5, 28-1-28-14

Slotboom, R.T., and Lawton, D.C., 1989, Depth-variant mapping and moveout correction of converted-wave data: CREWES project research report, v.1, 55-67

Slotboom, R.T., Eaton, D.W., and Lawton, D.C., 1990, Improving converted-wave (*P-S*) moveout estimation: CREWES project research report, v.2, 80-88

Tatham, R.H., and Stoffa, P.L., 1976, Vp/Vs - A potential hydrocarbon indicator: Geophysics, 41, 837-849

Tatham, R.H., 1992, Vp/Vs and lithology: Geophysics, 47, 336-344

Tatham, R.H., Goolsbee, D.V., Massell, W.F., and Nelson, H.R., 1983, Seismic shear-wave observations in a physical model experiment: Geophysics, 48, 688-701

Tatham, R.H., and Goolsbee, D.V., 1984, Separation of *S*-wave and *P*-wave reflections offshore western Florida: Geophysics, 49, 493-508

Tatham, R.H., and Stewart, R.R., 1994, Present status and future directions of shear-wave seismology in exploration: CREWES project research report, v.5, 1-1-1-22

Tessmer, G., and Behle, A., 1988, Common reflection point data-stacking technique for converted waves: Geophys. Prosp., 36, 671-688
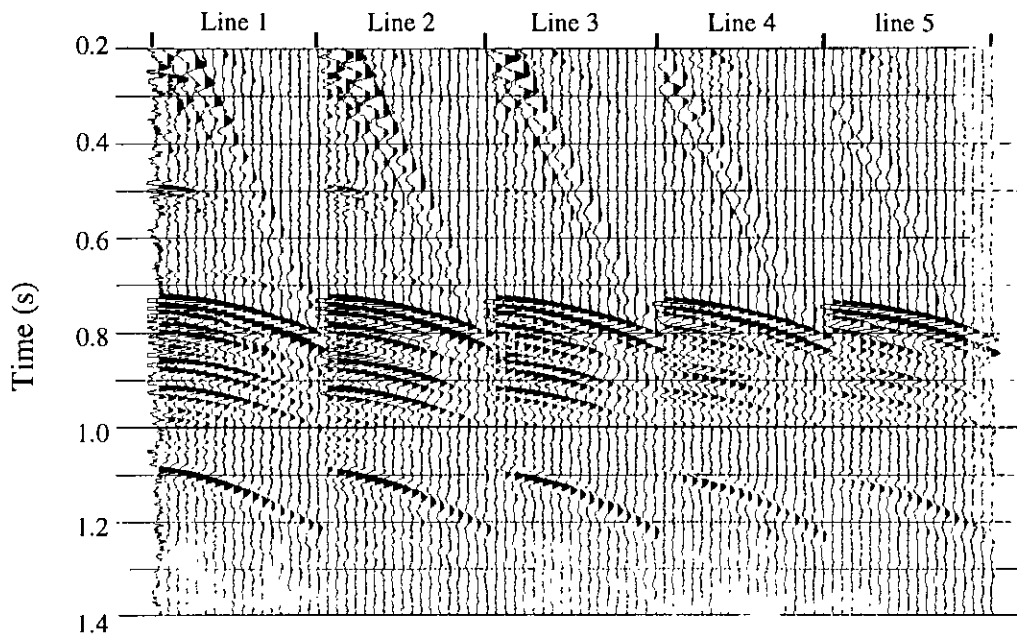
FIG. 7a. Example of in-line component *P-SV* data. Shot was at station 1 on shot-line 1.
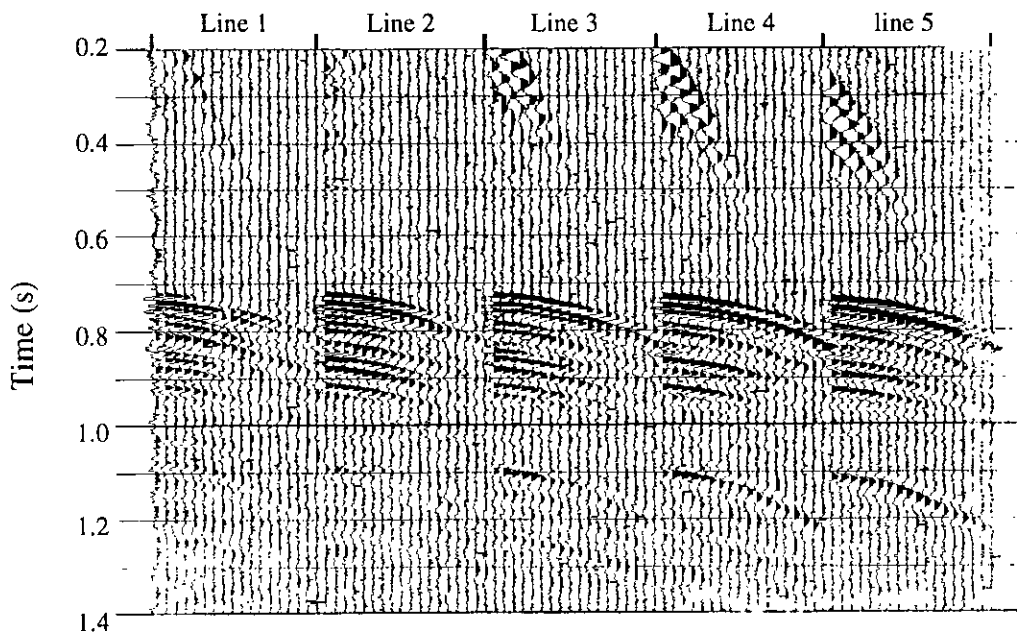
FIG. 7b. Example of cross-line component *P-SV* data. Shot was at station 1 on shot-line 1
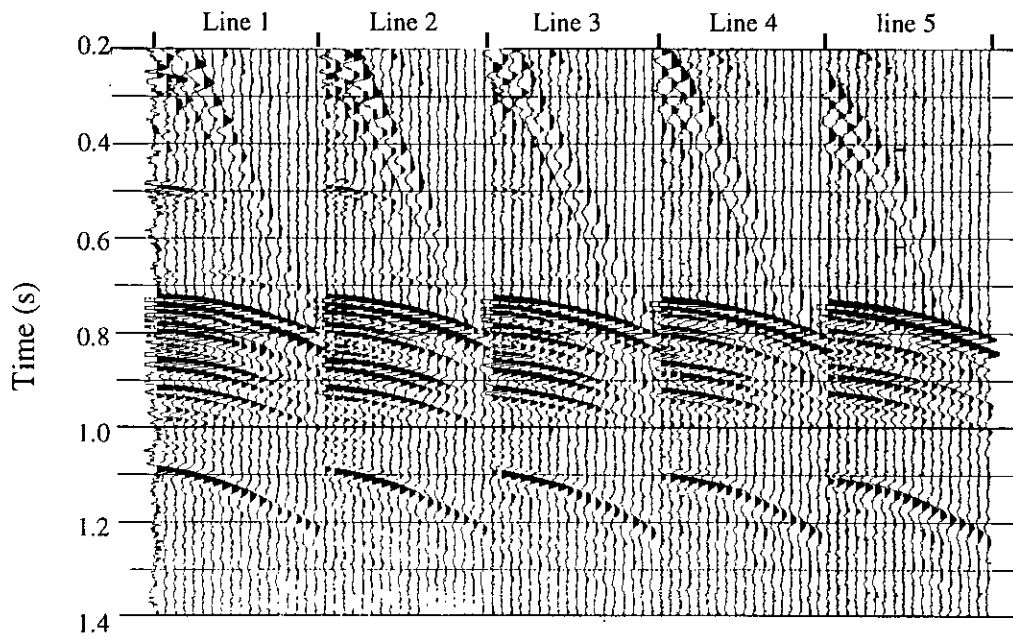
FIG. 8a. Example of radial component *P-SV* data. Shot was at station 1 on shot-line 1.
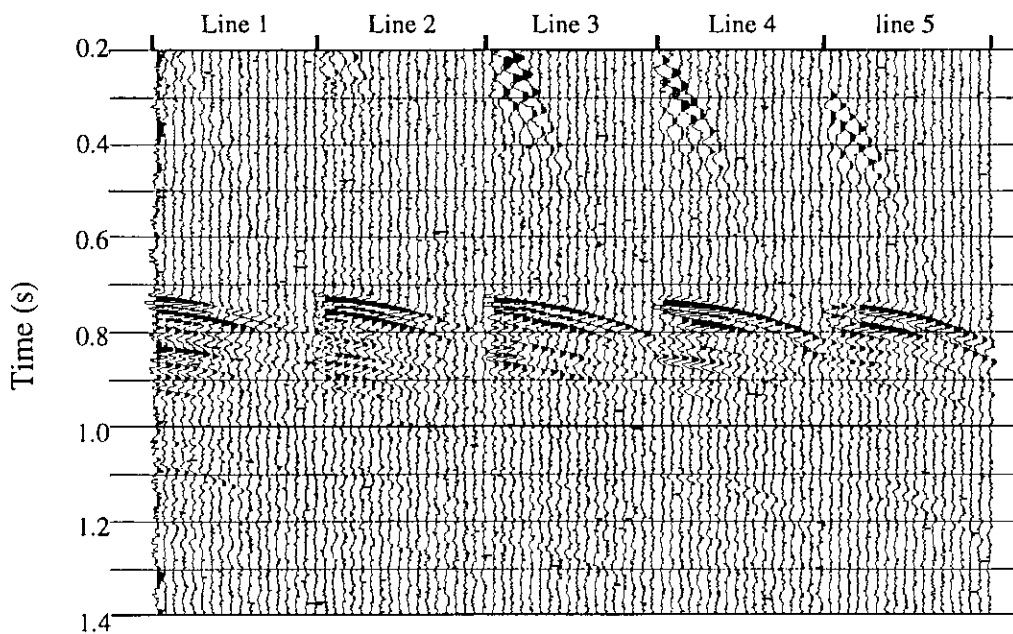

FIG. 8b. Example of transverse component *P-SV* data. Shot was at station 1 on shot-line 1
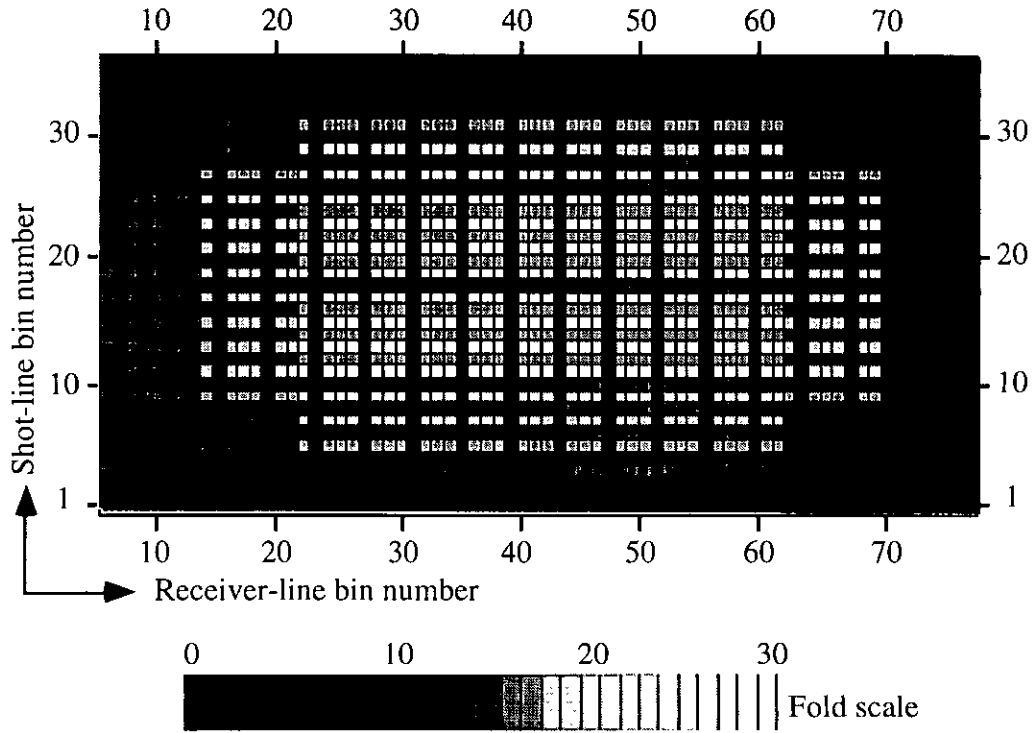
FIG. 10. Fold map of asymptotic common conversion point binning with bin size 25 m
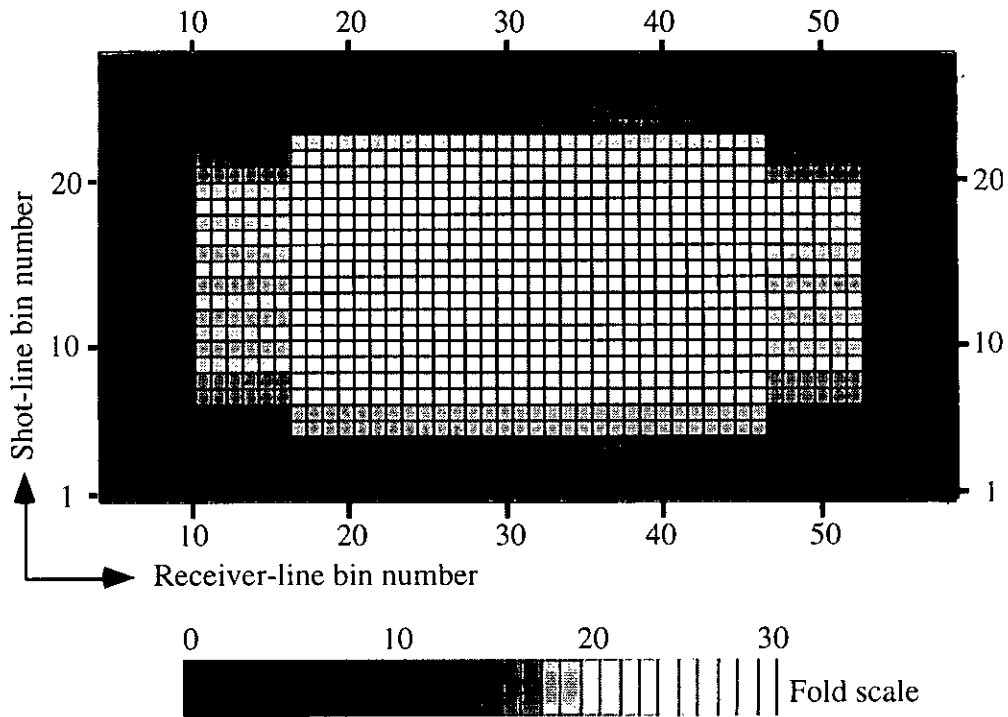
FIG. 11. Fold map of asymptotic common conversion point binning with optimum bin size 33.3 m
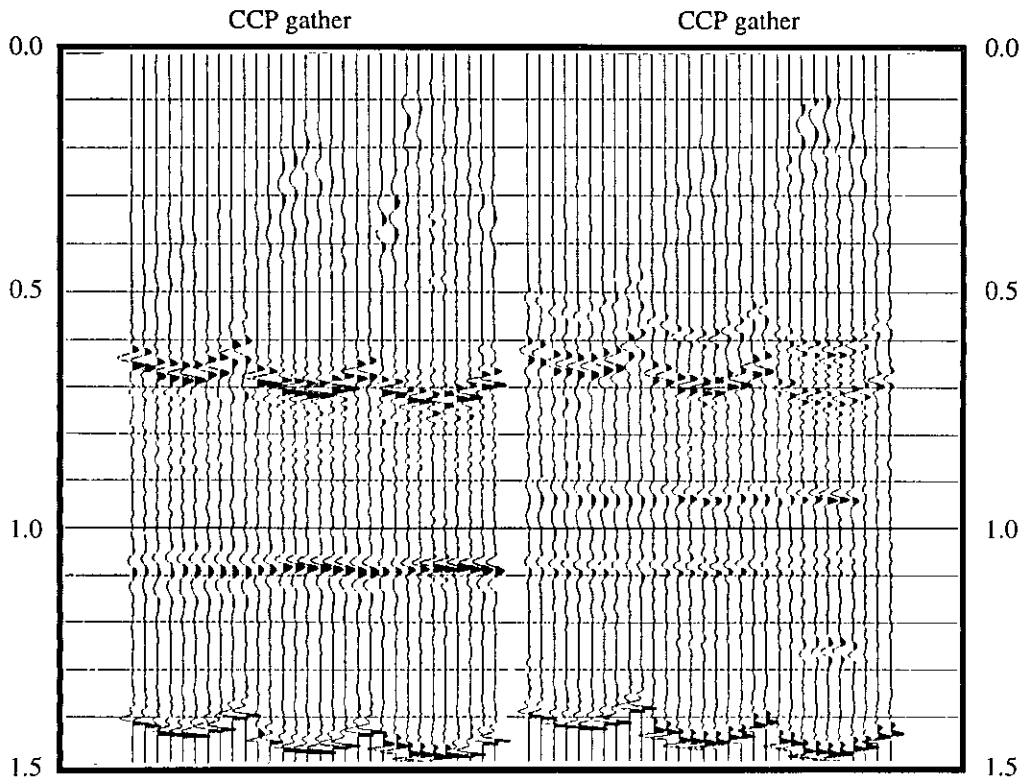
FIG. 12. Example of *P-SV* normal moveout correction using standard hyperbolic equation
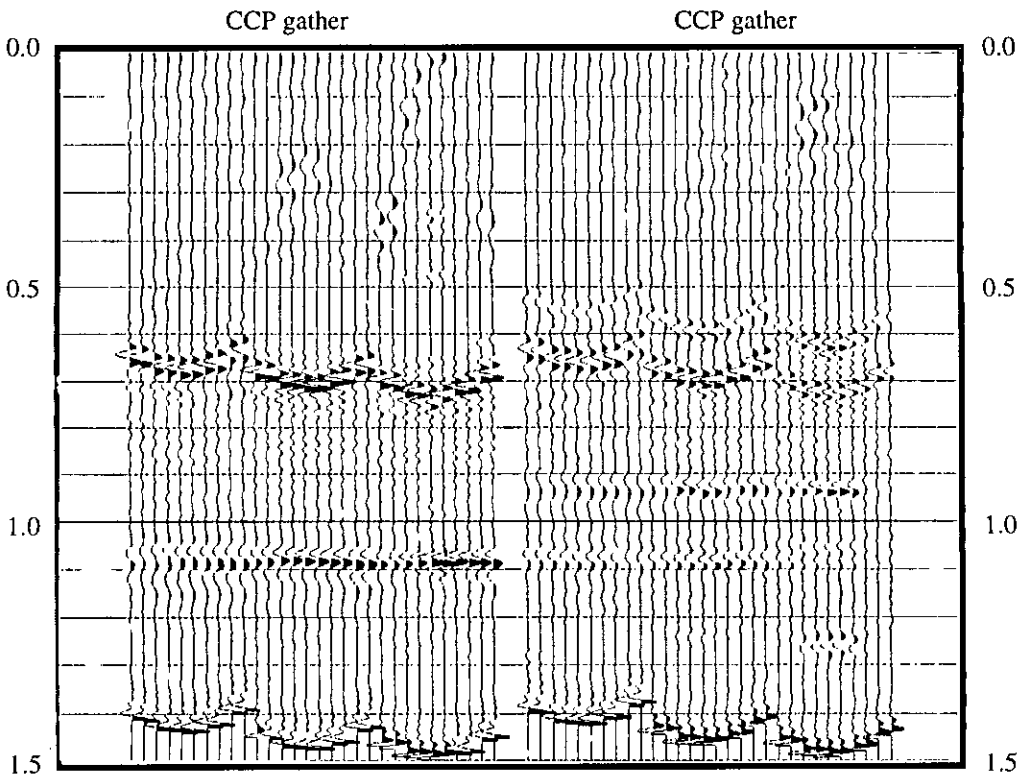
FIG. 13. Example of *P-SV* normal moveout correction using time-shifted hyperbolic equation
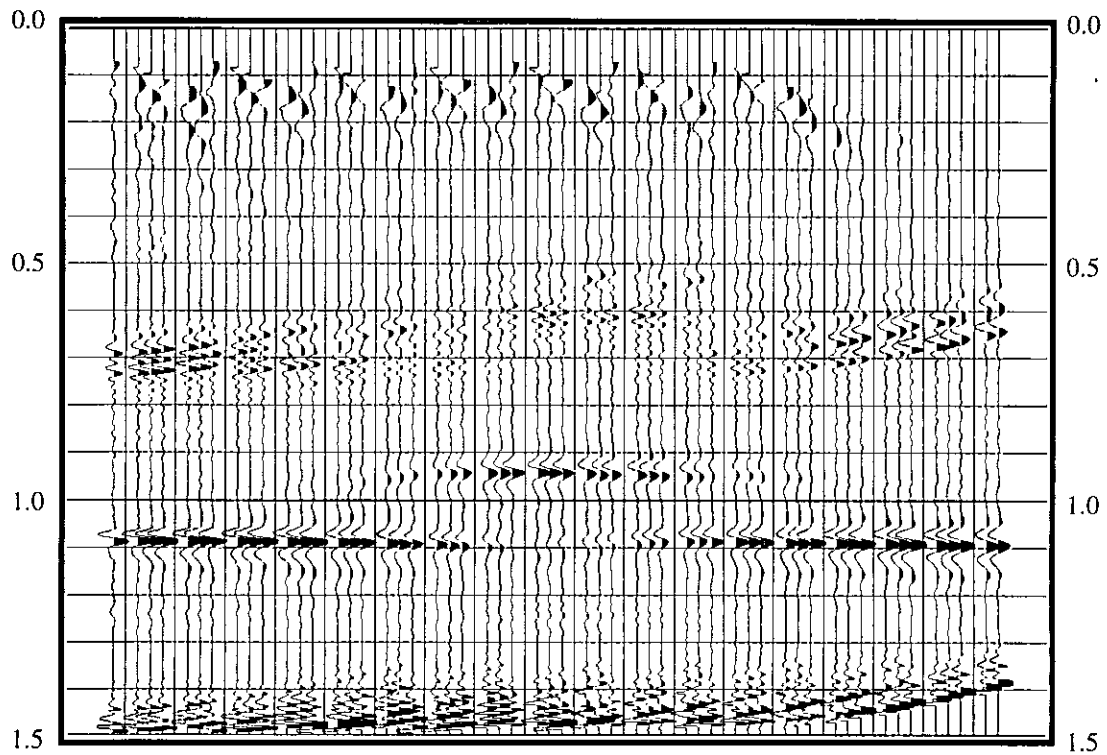
FIG. 14. Example section of *P-SV* stacked data in receiver-line direction with bin size 25 m, without interpolation of the empty traces.
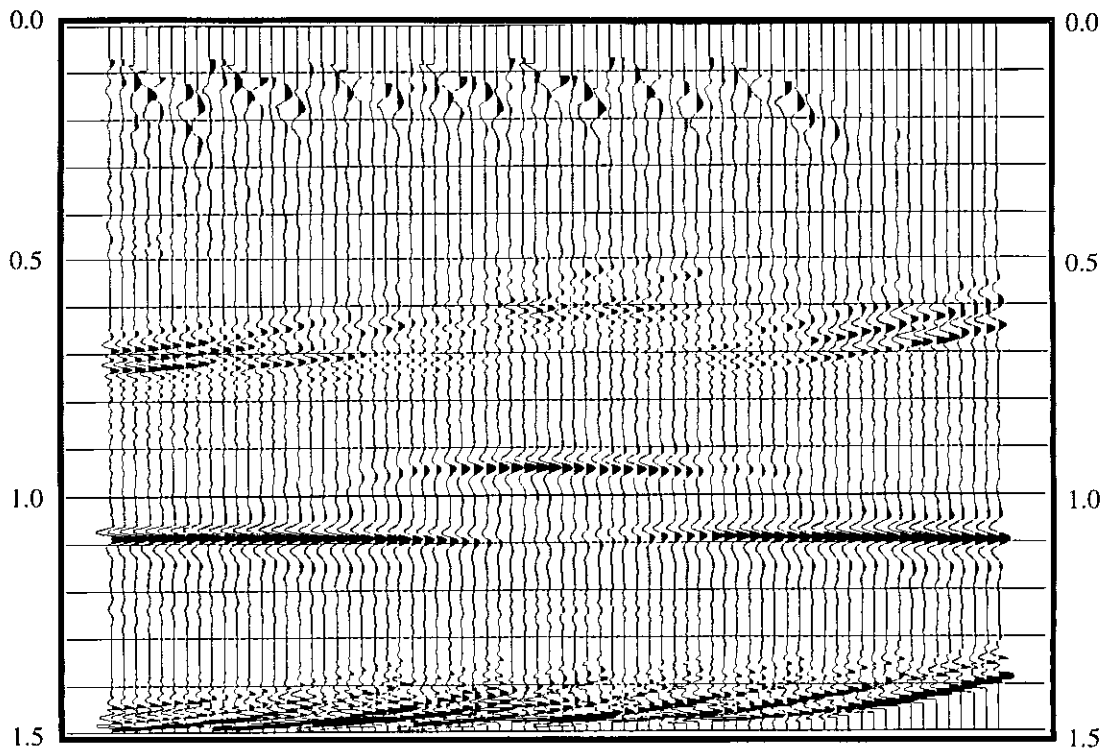
FIG. 15. Example section of *P-SV* stacked data in receiver-line direction with bin size 25 m, after interpolation of the empty traces.
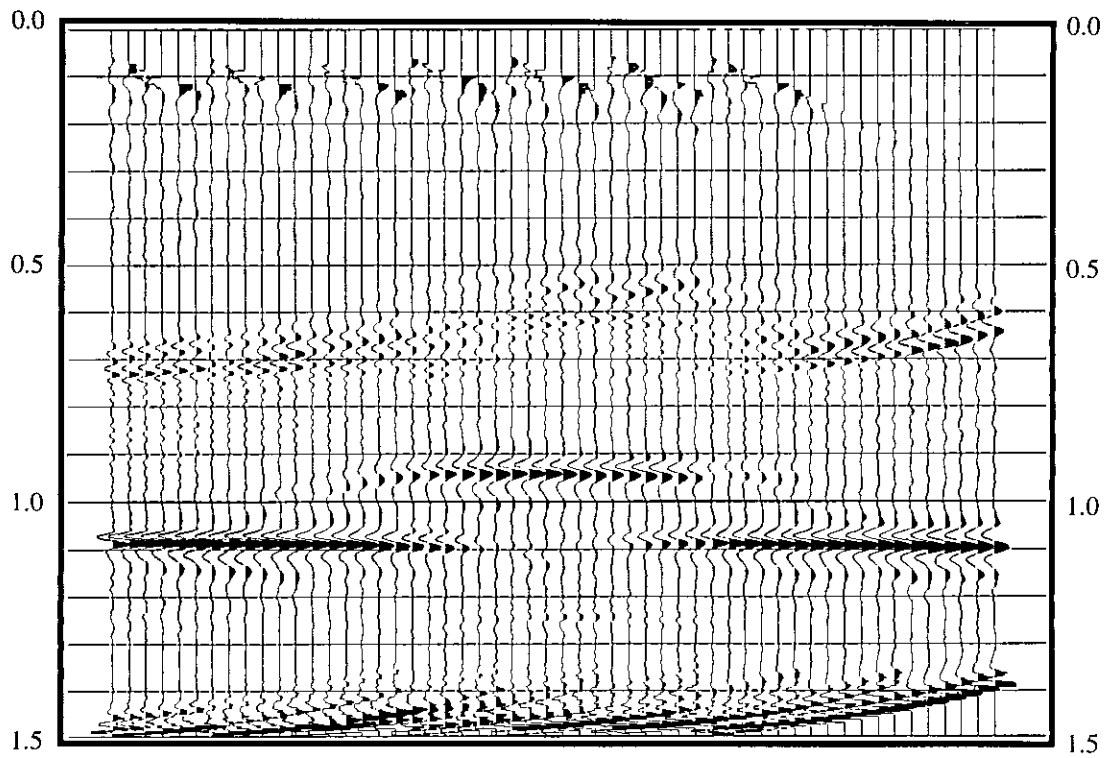
FIG. 16. Example section of *P-SV* stacked data in receiver-line direction with optimum bin size 33.3 m.

FIG. 17. Example section of *P-SV* stacked data in receiver-line direction with optimum bin size 33.3 m, then resample the data with bin size 25 m.
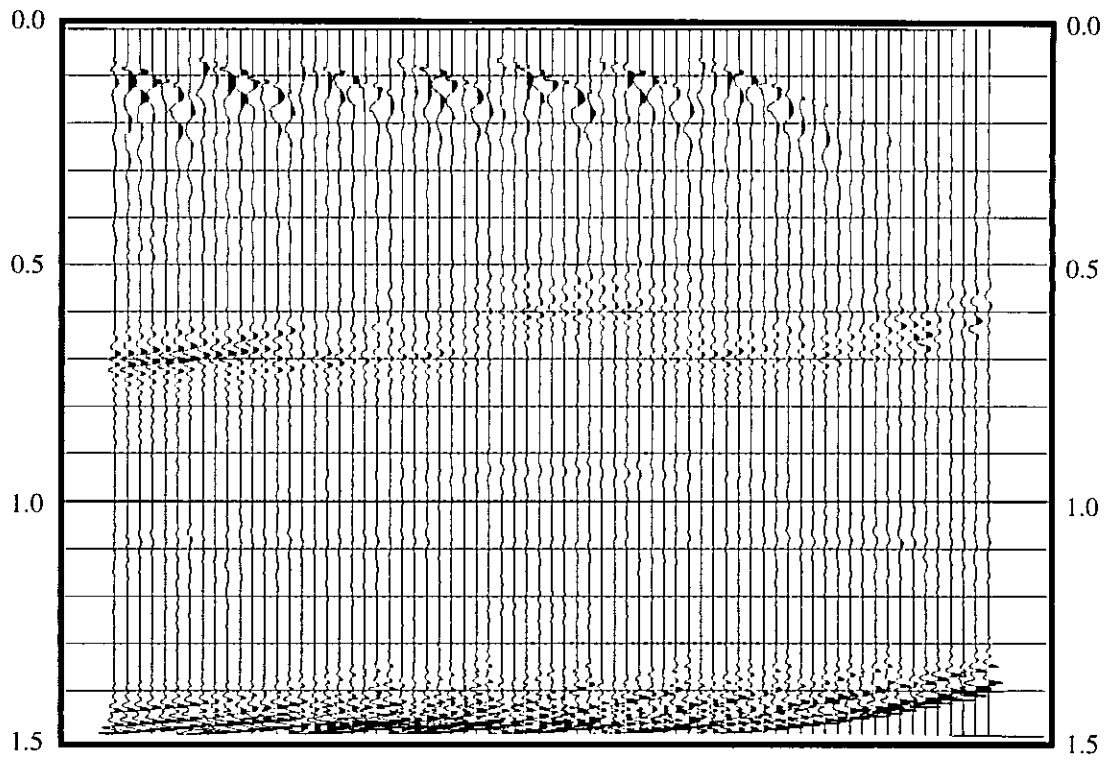
FIG. 18. The subtraction between Figure 17 and Figure 15.
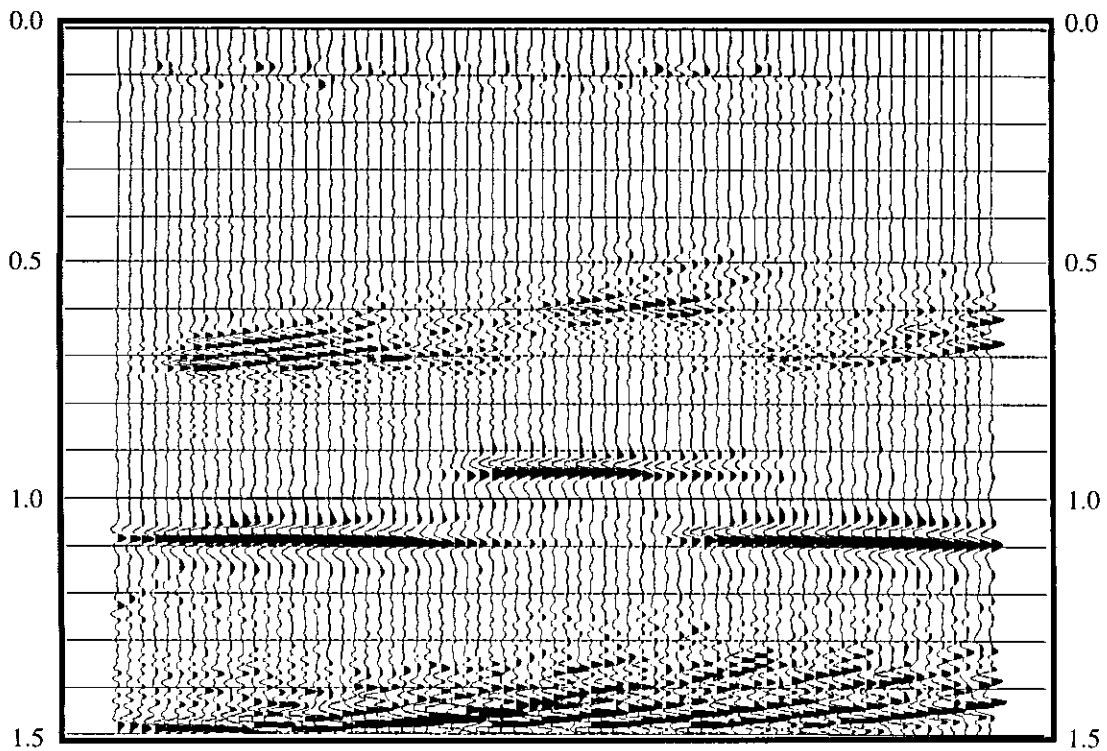
FIG. 19. Example section of *P-SV* migrated data in receiver-line direction after interpolation of the empty traces.
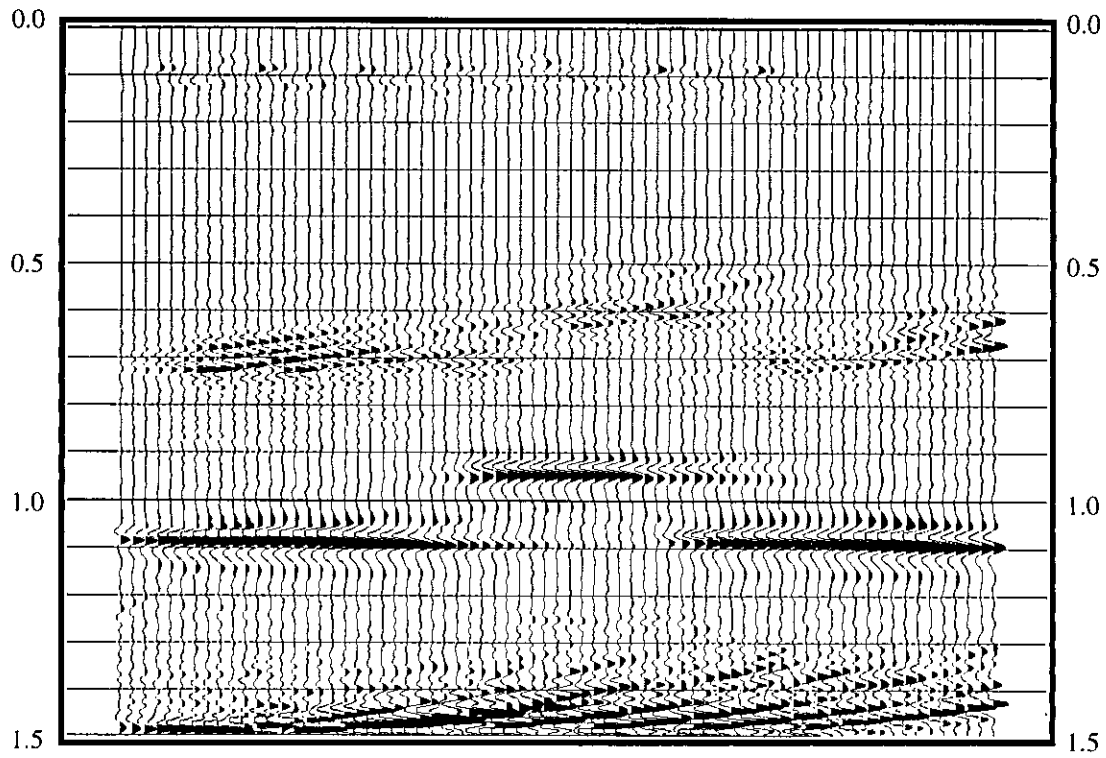
FIG. 20. Example section of *P-SV* migrated data in receiver-line direction with optimum bin size 33.3 m, after interpolating the data with bin size 25 m and migrating this data set.
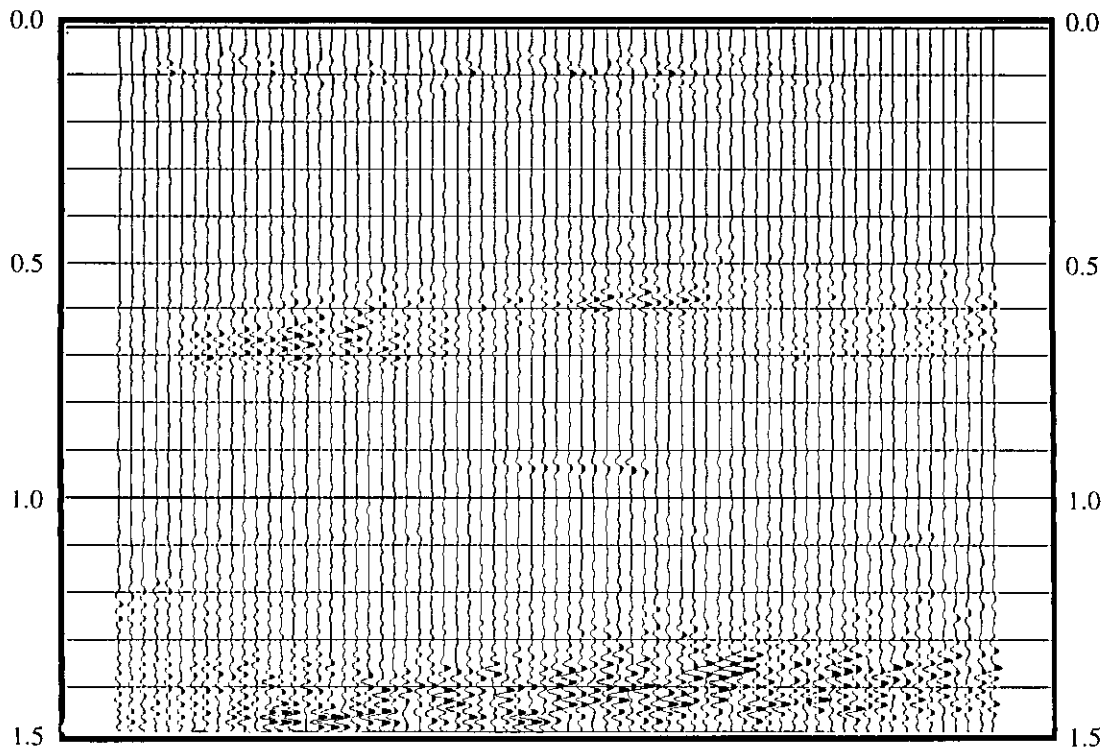
FIG. 21. The subtraction between Figure 20 and Figure 19.
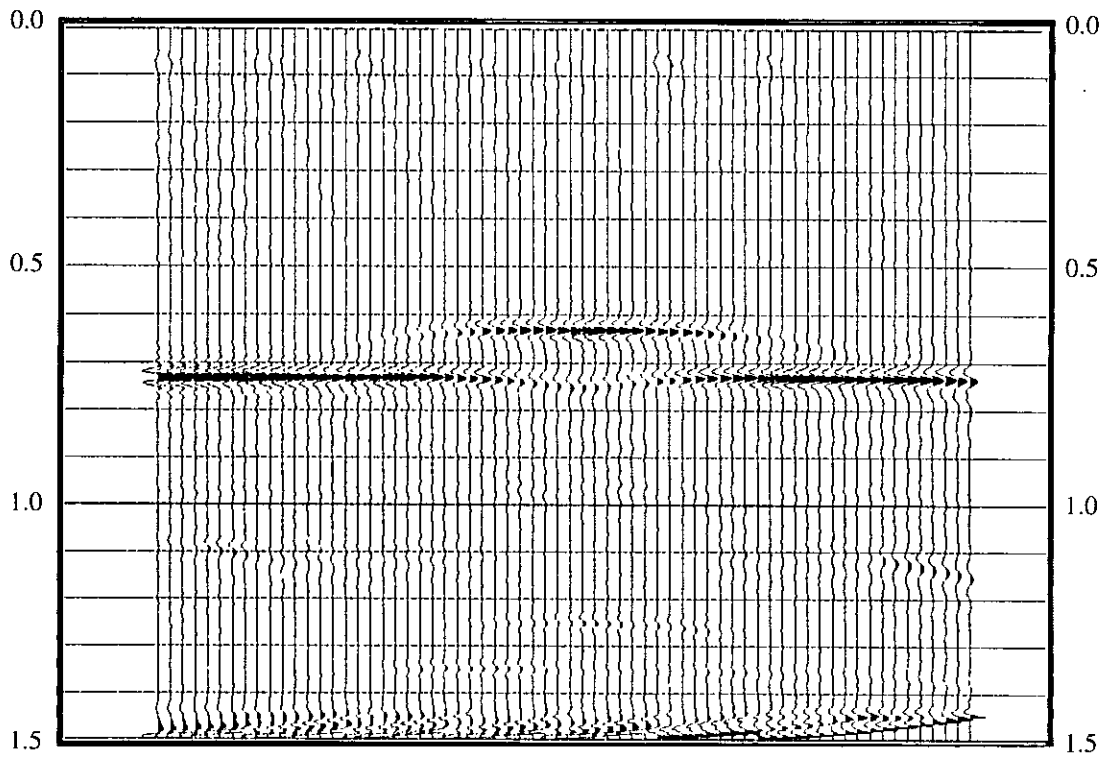
FIG. 22. Example section of *P-P* stacked data in receiver-line direction with bin size of 25 m
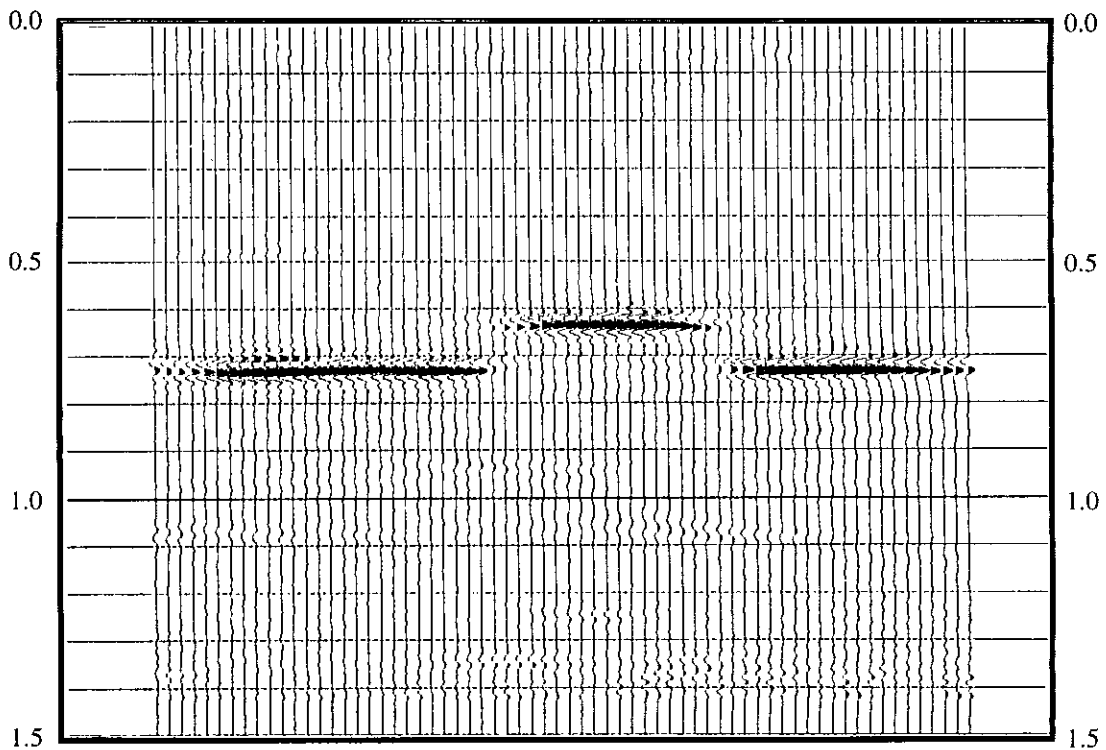
FIG. 23. Example section of *P-P* migrated data in receiver-line direction with bin size of 25 m.
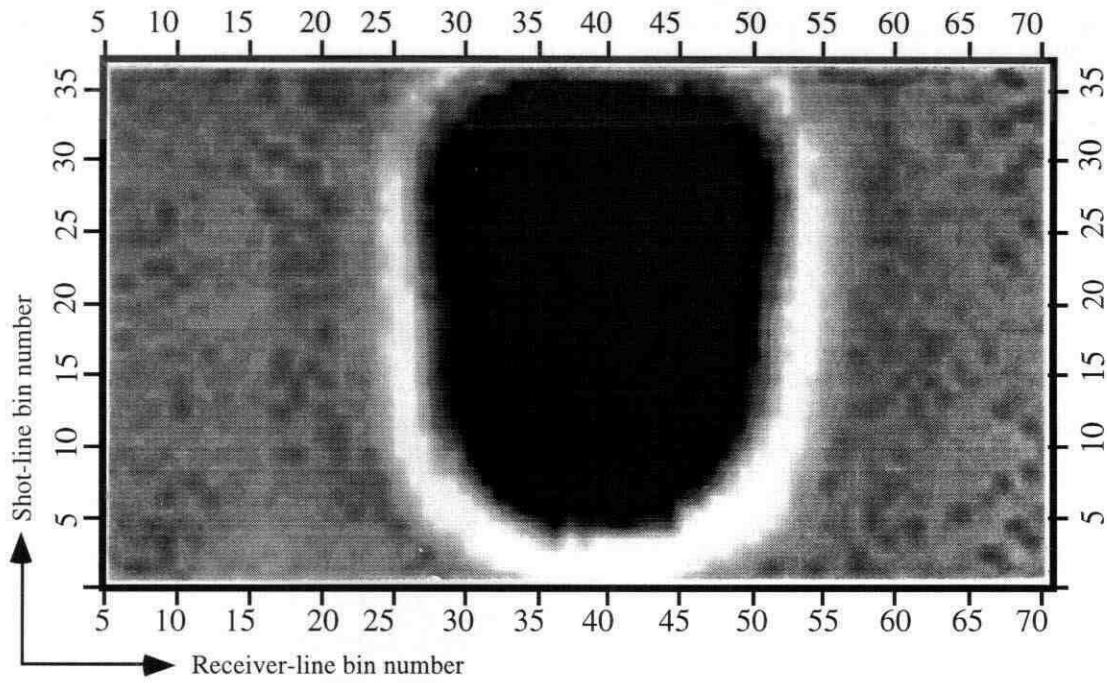
FIG. 24. Time slice of *P*-wave stacked data with time of 630 ms.
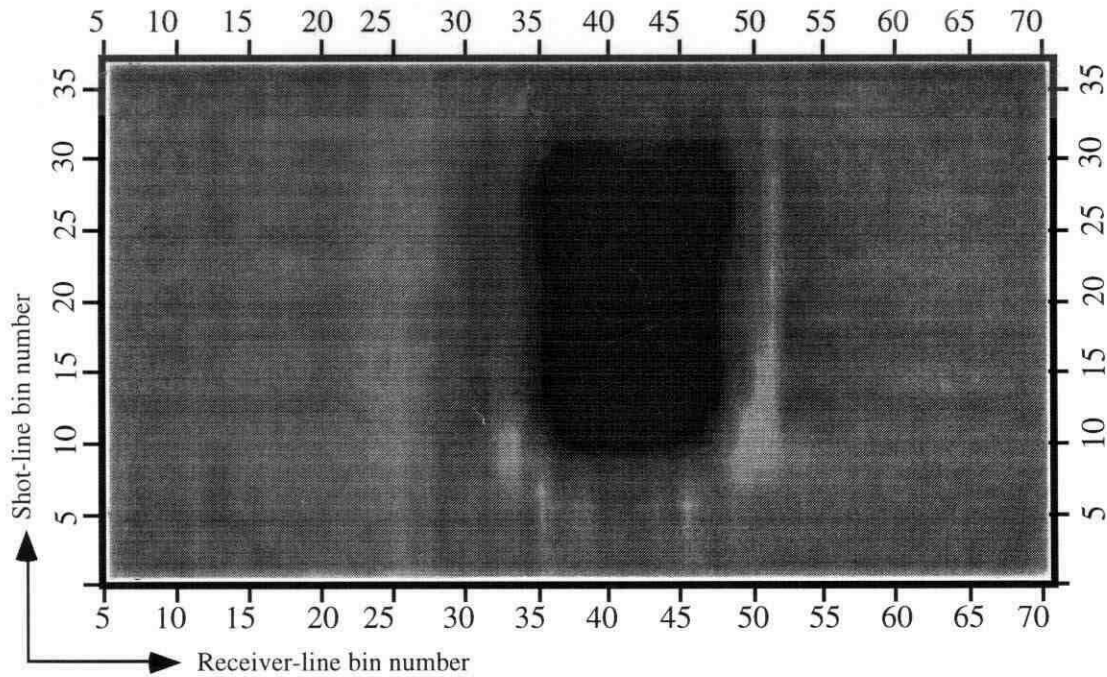
FIG. 25. Time slice of *P*-wave migrated data with time of 630 ms.
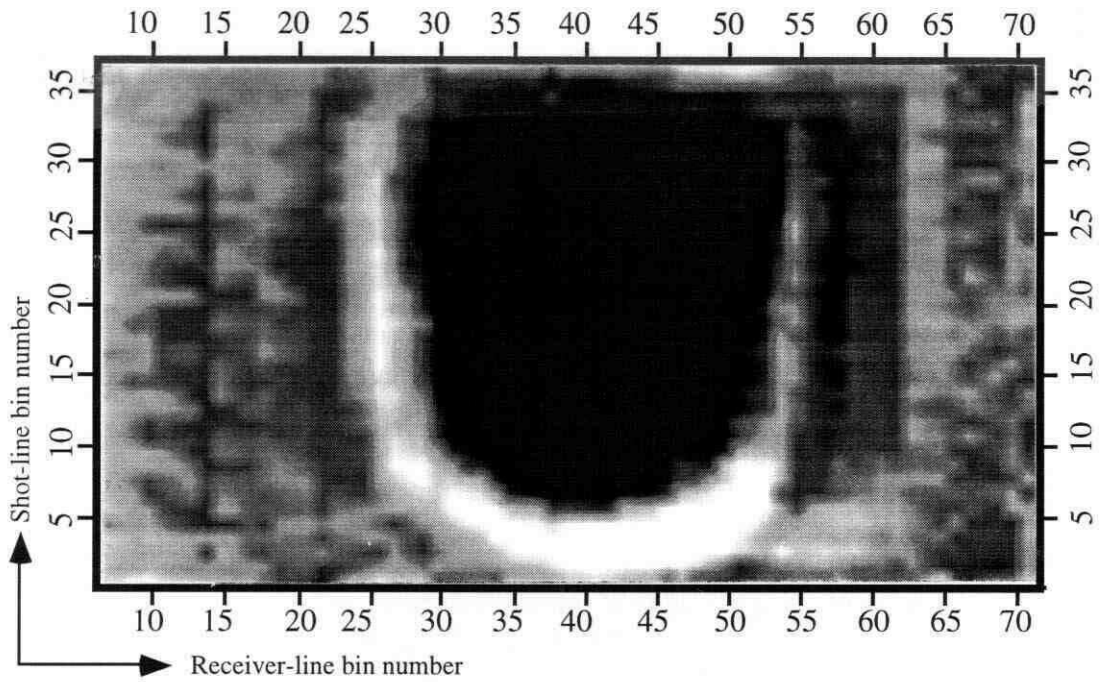
FIG. 26. Time slice of *P-SV* stacked data with time of 940 ms.
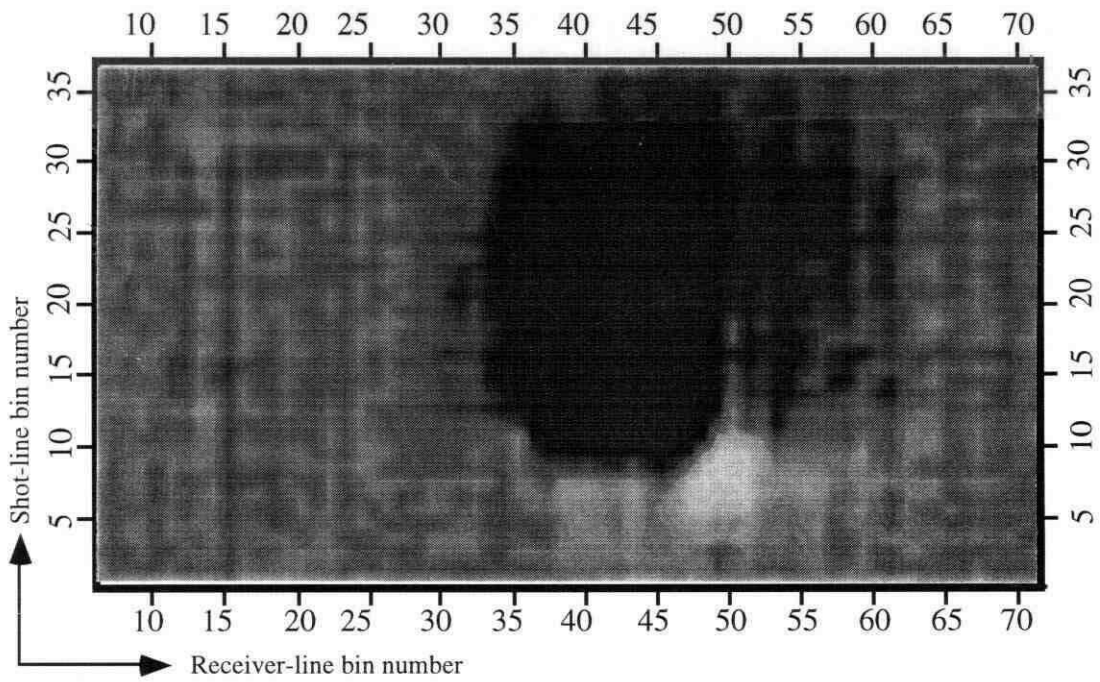
FIG. 27. Time slice of *P-SV* migrated data with time of 940 ms.
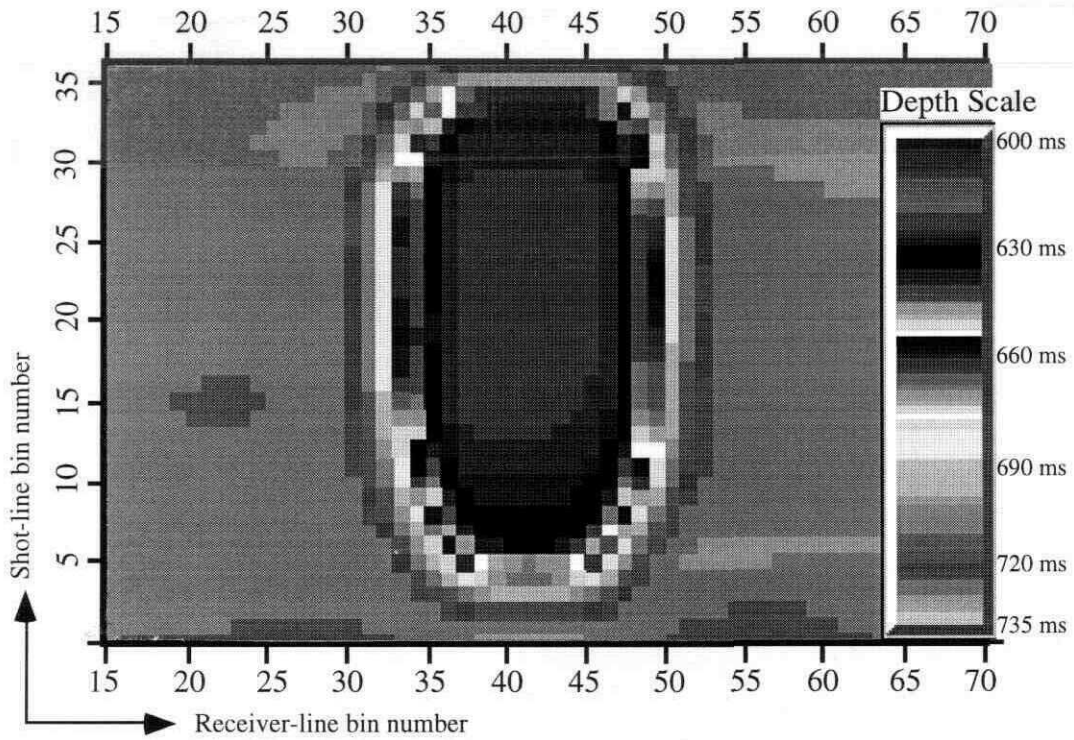
FIG. 28. Horizon map of *P*-wave migrated data from time 600 to 735 ms.
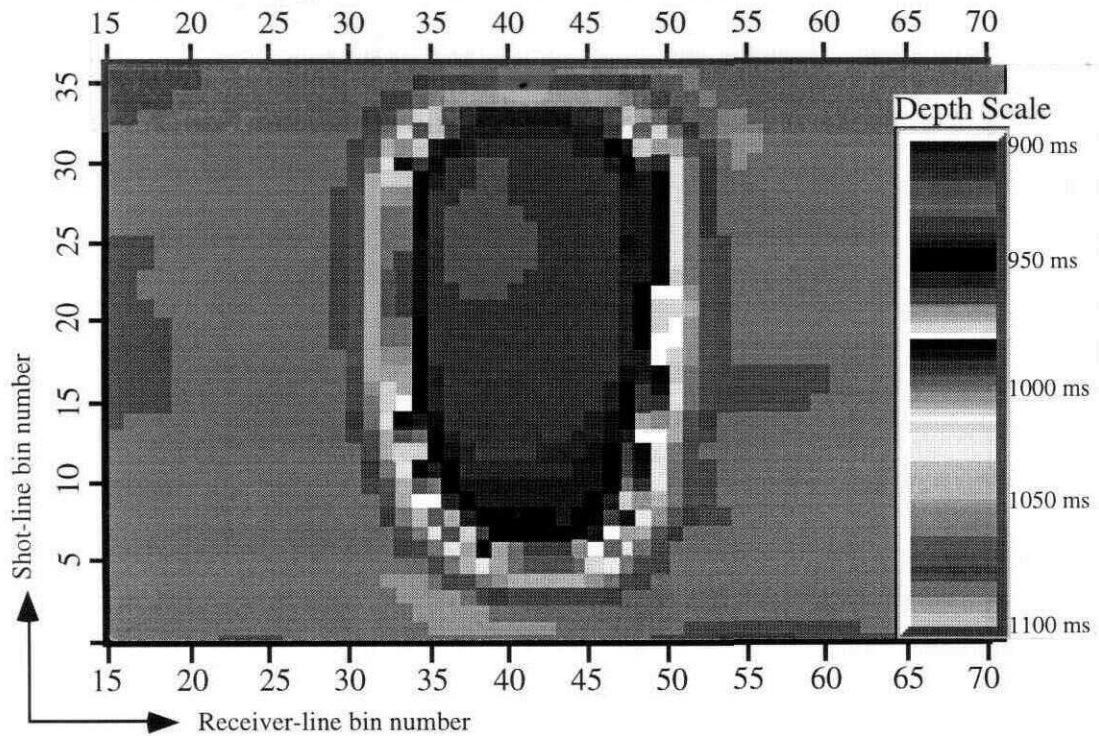

FIG. 29. Horizon map of *P-SV* migrated data from time 900 to 1100 ms.